remote sensing

MDPI

Article

A First Extension of the Robust Satellite Technique RST-FLOOD to Sentinel-2 Data for the Mapping of Flooded Areas: The Case of the Emilia Romagna (Italy) 2023 Event

Valeria Satriano [1,*], Emanuele Ciancia [1], Nicola Pergola [1] and Valerio Tramutoli [2]

[1] Institute of Methodologies for Environmental Analysis, National Research Council, Tito Scalo, 85050 Potenza, Italy; emanuele.ciancia@cnr.it (E.C.); nicola.pergola@cnr.it (N.P.)
[2] School of Engineering, University of Basilicata, 85100 Potenza, Italy; valerio.tramutoli@unibas.it
* Correspondence: valeria.satriano@cnr.it

Abstract: Extreme meteorological events hit our planet with increasing frequency, resulting in an ever-increasing number of natural disasters. Flash floods generated by intense and violent rains are among the most dangerous natural disasters that compromise crops and cause serious damage to infrastructure and human lives. In the case of such a kind of disastrous events, timely and accurate information about the location and extent of the affected areas can be crucial to better plan and implement recovery and containment interventions. Satellite systems may efficiently provide such information at different spatial/temporal resolutions. Several authors have developed satellite techniques to detect and map inundated areas using both Synthetic Aperture Radar (SAR) and a new generation of high-resolution optical data but with some accuracy limits, mostly due to the use of fixed thresholds to discriminate between the inundated and unaffected areas. In this paper, the RST-FLOOD fully automatic technique, which does not suffer from the aforementioned limitation, has been exported for the first time to the mid–high-spatial resolution (20 m) optical data provided by the Copernicus Sentinel-2 Multi-Spectral Instrument (MSI). The technique was originally designed for and successfully applied to Advanced Very High Resolution Radiometer (AVHRR), Moderate Resolution Imaging Spectroradiometer (MODIS), and Visible Infrared Imaging Radiometer Suite (VIIRS) satellite data at a mid–low spatial resolution (from 1000 to 375 m). The processing chain was implemented in a completely automatic mode within the Google Earth Engine (GEE) platform to study the recent strong flood event that occurred in May 2023 in Emilia Romagna (Italy). The outgoing results were compared with those obtained through the implementation of an existing independent optical-based technique and the products provided by the official Copernicus Emergency Management Service (CEMS), which is responsible for releasing information during crisis events. The comparisons carried out show that RST-FLOOD is a simple implementation technique able to retrieve more sensitive and effective information than the other optical-based methodology analyzed here and with an accuracy better than the one offered by the CEMS products with a significantly reduced delivery time.

Keywords: flood mapping; satellite data; Sentinel-2 data; Google Earth Engine

Citation: Satriano, V.; Ciancia, E.; Pergola, N.; Tramutoli, V. A First Extension of the RST-FLOOD Technique to Sentinel-2 Data for the Mapping of Flooded Areas: The Case of the Emilia Romagna (Italy) 2023 Event. *Remote Sens.* **2024**, *16*, 3450. https://doi.org/10.3390/rs16183450

Academic Editor: Fumio Yamazaki

Received: 02 August 2024
Revised: 12 September 2024
Accepted: 14 September 2024
Published: 17 September 2024

1. Introduction

Climate change is one of the main causes of the catastrophic natural events occurring on our planet: landslides, floods, fires, and extreme drought are now widespread phenomena that can be observed at any latitude. Among all these disastrous events, the flash floods generated by intense and violent rains are the most dangerous ones, occurring with destructive force and causing irreversible damage both in terms of economic consequences and the loss of human lives [1]. During the emergency phases linked to such a kind of event, a monitoring system able to retrieve timely information about the location

and extent of the affected areas is crucial for the authorities, in order to prioritize the right actions for containing and mitigating the impacts.

When the involved areas are not easily accessible by traditional ground surveillance systems, as usually happens in these cases, satellite observations may provide valid support. Several satellite techniques have been developed to detect and map flooded areas, using both active [2–8] and passive [9–18] sensors, with the ground resolution and accuracy of the final products being highly variable depending on the data source type and the performances of the methods. The satellite data to be used for this purpose are selected according to spatial (i.e., ground resolution) and temporal (i.e., revisit time) requirements. In addition to the data, the products' accuracy and timeliness must also be carefully considered and assessed. In particular, as far as the satellite products must be delivered during the emergency phase, completely automatic and unsupervised methods may speed up the analysis and significantly reduce the delivery time of the relevant information, which can then be available for end users and decision makers almost immediately after the satellite data acquisition.

The microwave data coming from active sensors provide a high spatial resolution (up to 5 m with no commercial satellite [19] products) and are generally available in *all* weather conditions with a temporal repetition of 6–12 days at mid-latitudes. However, the methodologies implemented for flood detection [2–6] are mostly semi-automatic, allowing for user-assisted products, whose accuracy is strictly dependent on the expertise of the operator [20,21]. Recently, a new study presented one of the first algorithms exploiting active microwave data, designed for monitoring flood events in a completely automatic way [7]: the algorithm was designed to work with Sentinel-1 Synthetic Aperture Radar (SAR) data, and it was operationally implemented in the Global Flood Monitoring (GFM) system and integrated in the Global Flood Awareness System (GloFAS) [22] and within the European surveillance system, the Copernicus Emergency Management Service (CEMS) [23]. The algorithm proved to be quite robust but needed to be improved to respond to the false alarms generated by seasonality effects, such as crop rotation in agriculture causing progressive land cover changes, which can produce signal backscattering variations erroneously interpreted as flood presence [7].

The satellite data acquired in the optical band, due to their own characteristics, can be more simply exploited in automatic applications for ground surveillance, even if these data can provide information only in cloud-free conditions [6,10,24]. The poor spatial resolution (from 1000 to 375 m) traditionally offered by the old generation of optical sensors (e.g., the Advanced Very High Resolution Radiometer—AVHRR; the Moderate Resolution Imaging Spectroradiometer—MODIS; and the Visible Infrared Imaging Radiometer Suite—VIIRS) typically used for this kind of application [11,25–29] has been significantly improved with the launch of the new generation of sensors operating aboard the last Earth Observation (EO) missions (e.g., the Copernicus Sentinel platforms). These sensors provide a spatial resolution up to 10 m in the visible channels [30] together with a revisit time that, thanks to the constellation of two twin satellites, allows for a new image in 5 days on average. The advent of such data has allowed the development of new techniques for flood detection and monitoring [15–18] that are more accurate than previous ones and with an ever-increasing degree of automation. Despite this, they show some limits when implemented at a global scale, due to the need for ancillary information not always and not everywhere available [17] and/or because of the employment of fixed, non-adaptive thresholds [15,16], which may lead to a significant reduction in accuracy when exported to different geographic environmental/observational conditions.

The official European EO-based emergency service currently in charge to provide information worldwide during an emergency phase related to different kind of disasters (e.g., floods) works with different observation data and models in order to overcome the principal limits linked to data availability. This service is the CEMS [31], a global on-demand service to support the actors involved in the management of disasters (e.g., national/regional civil protection offices and local/regional authorities); the goal is

producing timely (rapid mapping) [32] and accurate (risk and recovery) [33] products useful for the different crisis phases.

In this study, an existing fully automatic optical technique, namely RST-FLOOD [34], has been ported for the first time to the Copernicus Sentinel-2 Multi-Spectral Instrument (MSI) data. The technique, which by its construction does not exploit fixed thresholds, was originally proposed for and successfully implemented on mid–low-spatial resolution (300 m–1 km) satellite data [11,35]. Here, it has been exported for the first time to mid–high-resolution (20 m) Sentinel-2 data. The selected study case is the devastating flood event that occurred in May 2023 in Emilia Romagna (Italy), with 23 rivers overflowing, huge economic damage, and several injuries. The quality of the results obtained were evaluated and discussed compared with the same arising from another existing satellite optical technique proposed in [16] and the microwave-based products provided by the official CEMS service.

2. Materials and Methods

In this section, information about the flooding event analyzed, the satellite data, and the existing products used are reported. RST-FLOOD and the techniques from [16] implemented in this work to the specific study case are then fully described.

2.1. The Emilia Romagna (Italy) Flooding Event of May 2023

The study area selected in this work is the Emilia Romagna region in Italy (Figure 1a), which was affected by two intense flooding events that occurred during the month of May 2023.

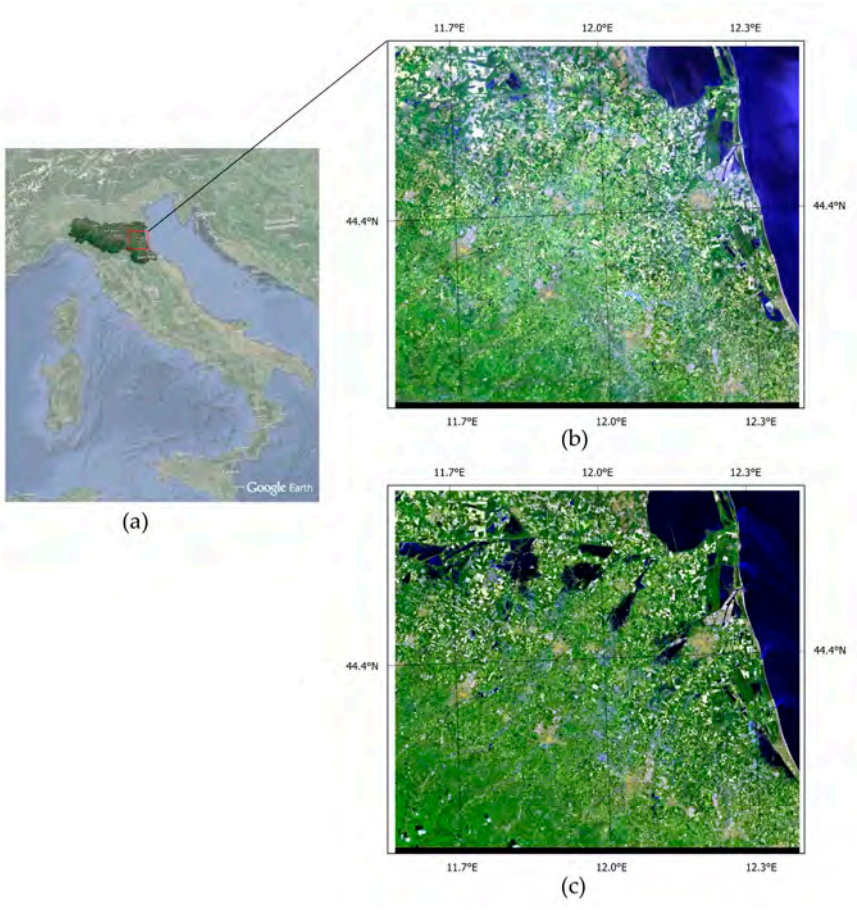

Figure 1. (**a**) Emilia Romagna region (Italy); Sentinel-2 false color RGB (R = 2.1 μm, G = 1.6 μm, and B = 0.49 μm) images of the study area acquired on (**b**) 28 April 2023 (pre-event) and (**c**) 23 May 2023 (post-event).

Emilia Romagna is a highly vulnerable area to flood risk due to its arrangement and to the presence of a complex system of drainage canals and watercourses [36]. In May 2023, the region was hit by severe rainfall: the first one occurred on 2 May and was defined as the worst (over 200 mm of precipitation in 48 h) in the region since 1997 [36], causing the first floods in the area. Afterwards, two even more intense episodes affected the region, leading to a second destructive flood event on 16 May. The latter caused 23 rivers and waterways to overflow [37], the death of 15 people [38], and the evacuation of over 36,000 citizens [39].

2.2. Data and Processing Techniques

2.2.1. Satellite Data and Products Used

The satellite data acquired by the Sentinel-2 MSI were used in this work to implement the RST-FLOOD detection scheme together with the independent optical technique recently proposed in [16] (hereafter mentioned as CAB). The MSI images were chosen for the purpose because they are presently the best compromise between spectral, spatial, and temporal resolutions among all the optical satellite data currently freely distributed. Sentinel-2 is a multi-spectral optical mission for the high-resolution monitoring of the Earth [40], counting on two platforms (i.e., Sentinel-2A and 2B) and offering 10 days of revisit time in the single satellite configuration and 5 days in the constellation. The MSI sensor is on board both satellites, providing multi-spectral imagery collected in 13 spectral bands (from Visible (VIS) to Short-Wave Infrared (SWIR)), with the spatial resolutions ranging from 10 m to 60 m [41]. Sentinel-2 provides different data products [42]: Top Of Atmosphere (TOA) radiance (i.e., Level 1B–L1B data) and reflectance (i.e., Level 1C–L1C data), in addition to Bottom Of Atmosphere (BOA) reflectance, renamed as Surface Reflectance (i.e., Level 2A–L2A data), obtained running the *sen2cor* model to correct the data from atmospheric contributions [43].

The first Sentinel-2 cloud-free (i.e., no clouds over the flooded areas) image available for the study area after the 16th of May event was the one acquired on 23 May 2023, which is reported in false color (R = 2.1 μm, G = 1.6 μm, and B = 0.49 μm, resampled at 10 m for the spatial resolution) in Figure 1c. This image was used as the source image for both the CAB and RST-FLOOD techniques here implemented. A second pre-event image, acquired on 28 April 2023 and reported in the same false color of the previous one in Figure 1b, was selected and used as representative of unperturbed conditions over the area for the CAB implementation.

As already mentioned, the official CEMS products freely provided through the official website [31] were used in this work to carefully assess the methodology presented. The CEMS service was activated by the authorities for the Emilia Romagna event in the rapid mapping mode on 16 May 2023 [44,45], providing the first information through the delineation product. This product is a timely (18–34 h for delivery) floods map of the whole area obtained from the SAR images, implementing semi-automatic techniques: in Figure 2, the relative map as of 21 May 2023 is shown. During the emergency phase, the authorities also defined specific areas of interest (AOIs) (Figure 3) to pay attention to [46], which have been used in this work to identify the most affected areas.

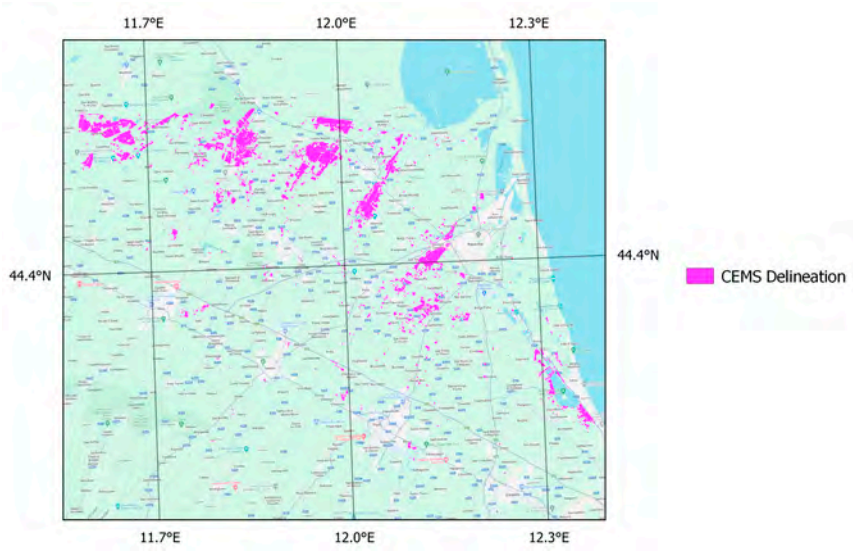

Figure 2. Delineation product flood areas (in purple) as of 21 May 2023. The Google Maps (world map service-WMS version) scene is used as the background.

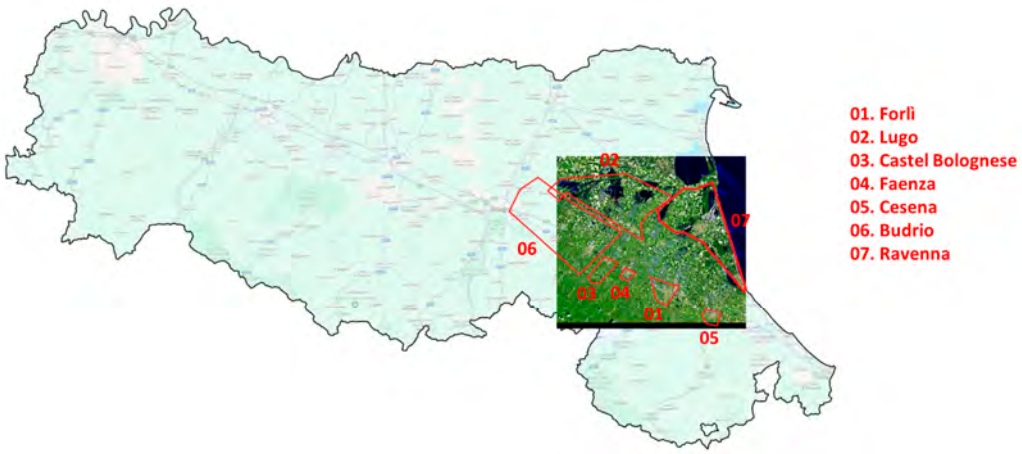

Figure 3. Emilia Romagna region with the Sentinel-2 post-event image superimposed. The red polygons are the different AOIs defined by the authorities.

Due to the size of the Emilia Romagna event and its related damage, a second CEMS phase was activated, i.e., *risk and recovery* (R&R), to obtain a more precise and detailed estimation of the flooded areas necessary to start recovery actions [45]. The relative flood delineation product was obtained by processing the Sentinel-1 SAR image acquired on 23 May 2023 through a supervised random forest classification, which was finally validated by an operator [45]. The product was released two months after the event, starting on 11 July 2023, and it is shown in Figure 4, which follows.

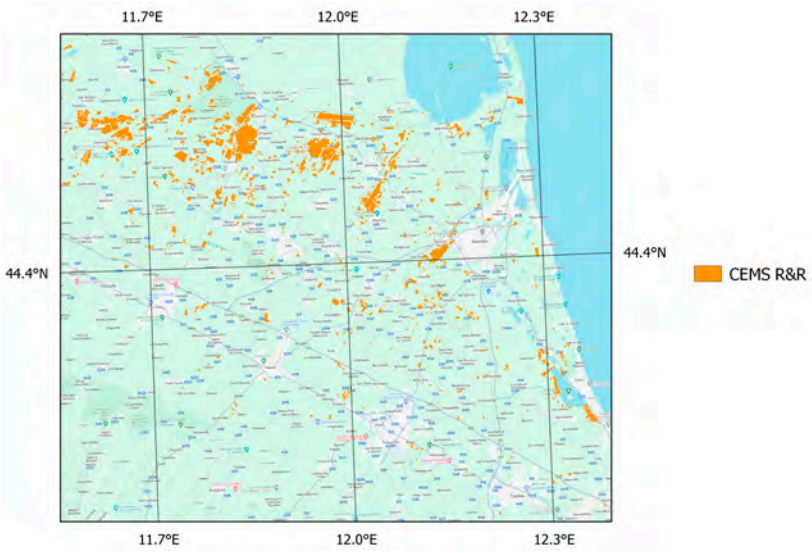

Figure 4. The risk and recovery (R&R) flood areas (in orange) as of 23 May 2023. The Google Maps (world map service-WMS version) scene is used as the background.

2.2.2. RST-FLOOD

The RST-FLOOD [34] technique, here exported for the first time to the Sentinel-2 data, is built on the Robust Satellite Technique (RST) [47] general approach: it is based on a statistical characterization of the observed satellite signal, performed through the study of a historical dataset of satellite images acquired in homogeneous conditions (i.e., with the same spectral signal, same geographic location, and same sensing period). This statistical characterization, carried out at pixel level, leads to the definition of the normal signal behavior, which will be considered as a reference of unperturbed conditions and defined through the so-called reference fields: (i) the expected value (i.e., the temporal mean—μ) and (ii) the normal variability (i.e., the standard deviation—σ). According to the RST prescriptions, any statistically significant signal deviation can be evaluated, at pixel level, by measuring the excess between the signal at hand and its expected value, then weighed with respect to its normal variability.

In detail, for the implementation to the flooded areas mapping, the chosen signal is the value resulting from the combination of the two spectral bands calculated through a diagnostic index, the Normalized Difference Snow Index (NDSI) [34]. This parameter was identified in [34] because it offers the best trade-off between reliability and sensitivity with respect to the other metrics analyzed [34]. The NDSI computes the normalized difference between the reflectance measured in the RED (0.6 μm) and Short-Wave Infrared (SWIR) (1.6 μm) bands, i.e., (RED-SWIR)/(RED+SWIR). Although first proposed to identify snow coverage [48], it is also able to emphasize the different spectral behavior of the flooded/non-flooded areas expected in these bands as deeply explained and discussed in [34]. In summary, the presence of turbid waters (i.e., rich in sediments) leads to a signal increase in the RED band and a decrease in the SWIR channel (which is more affected by water absorption), with a resulting positive difference between the two. On the other hand, in the absence of water, for all the soil and vegetation cover, this difference is expected to be negative.

To analyze the Emilia Romagna flood event, the RST-FLOOD process chain was implemented within the Google Earth Engine (GEE) [49] through an ad hoc JavaScript code created to perform the operations described below. Exploiting the open archives available in the platform cloud, a historical dataset of the Sentinel-2 MSI L2A data over the study area was built according to the RST requirements: all the images available within the GEE for the month of May were collected, analyzing a six-year period (2017–2022). The dataset obtained was composed of a total of 70 satellites. An accurate and original cloud mask

procedure was then implemented at the pixel level using three different steps: (i) a first masking phase was carried out using the QA60 quality band, available only till 2021, and the Sentinel-2 Cloud Probability collection to filter the 2022 data. The QA60 is a bitmask band available in the Sentinel-2 MSI data stream [50,51], while the Sentinel-2 Cloud Probability is a separate collection, available within the GEE, which provides the probability at pixel level to be covered by clouds [52]. (ii) A second cloud mask step was implemented in order to refine the output: the pixels flagged as clear in the previous phase were processed through the RST-based one-channel cloud detection approach (OCA) method [53], in order to obtain a more accurate output. (iii) The last step involved the pixels that passed the previous phases, and it was a cloud shadow mask, i.e., a procedure that is able to recognize and filter out cloud shadows through the use of the solar azimuth angle.

For each of the images collected and thus filtered, the NDSI index was then computed using MSI band 11 (at 1.6 μm) automatically resampled by the GEE to 10 m for the spatial resolution and band 4 (at 0.6 μm) with 10 m for the spatial resolution, obtaining a historical dataset of the NDSI maps of the area under investigation. Starting from this stack of NDSI maps, the above-defined reference fields, i.e., $\mu_{NDSI}(x,y)$ and $\sigma_{NDSI}(x,y)$, were computed. Afterwards, to assess the statistical significance of the deviations between the NDSI*(x,y,t)*, measured at time *t* at a single pixel *(x,y)* and the expected value for the same location, $\mu_{NDSI}(x,y)$, the Absolutely Local Index of Change of Environment (ALICE) [47] was computed as follows:

$$\otimes_{NDSI}(x,y,t) = \frac{NDSI(x,y,t) - \mu_{NDSI}(x,y)}{\sigma_{NDSI}(x,y)} \quad (1)$$

where NDSI*(x,y,t)* is the snow index value measured at a pixel *(x,y)* of the image under consideration acquired at time *t* and $\mu_{NDSI}(x,y)$ and $\sigma_{NDSI}(x,y)$ are the above-described reference field values computed for the same pixel analyzing the whole dataset of homogeneous NDSI maps. Considering that the ALICE index, in its construction, follows a standardized quasi-Gaussian distribution (with $\mu = 0$ and $\sigma = 1$) (see, for instance, [54]), the value it returns can identify the occurrence of statistically anomalous events [55]. As mentioned before, the anomalous presence of turbid water on the ground is associated with positive $\otimes_{NDSI}(x,y,t)$ values. In particular, $\otimes_{NDSI}(x,y,t)$ index values greater than 2, with a very low occurrence probability (2.27%), can reveal statistically significant anomalies that are likely to refer to inundated locations. A simplified scheme of RST-FLOOD as just described is reported in the following Figure 5.

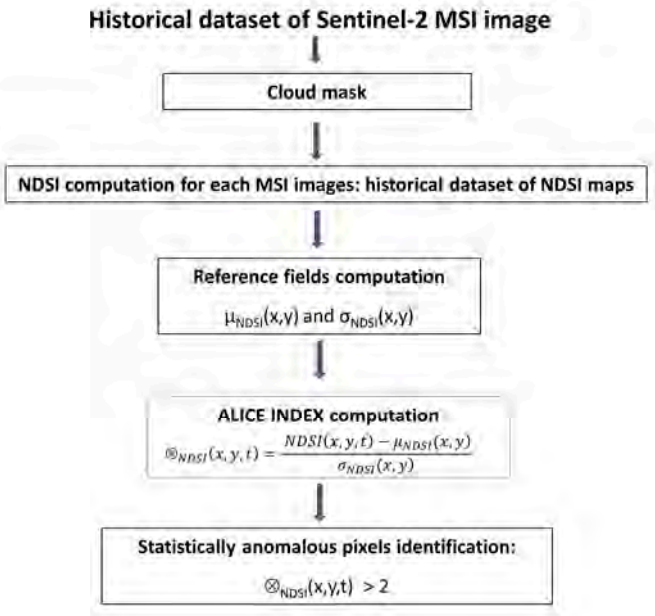

Figure 5. RST-FLOOD simplified scheme. The whole procedure reported was carried out at pixel level.

The above-described RST-FLOOD process implemented within the GEE [49] is completely automatic and unsupervised, does not need ancillary data, does not exploit fixed thresholds, and is able to generate the final product (i.e., anomalous pixels delineating the map of inundated areas) in only 15 min (starting from the availability of the image at time t to be investigated). The use of only satellite data makes the technique site-independent; moreover, its construction within the GEE environment allows a fast and simple implementation of the technique itself wherever it is necessary.

2.2.3. The [16] Technique

The CAB technique [16] is a Sentinel-2 MSI-based procedure to map flooded areas by using a combination of different spectral tests on the atmospherically corrected remote sensing reflectance, Rrs(λ) (L2 data). Operationally, the Sentinel-2 MSI Level 1C (S2/MSI-L1C) data were downloaded from the European Space Agency (ESA) official science hub [56] for the area of interest (Figure 1b,c) for the April–May 2022 period. Only the S2/MSI-L1C data characterized by the same orbit track (with R022 and 32TQQ as the orbit and tile numbers, respectively) and 20% maximum cloud coverage were retained for the subsequent L2 data processing. Among these data, the S2/MSI images of 28 April 2023 and 23 May 2023 were assumed to be the reference and target ones, respectively.

Then, the ACOLITE-based L1 to L2 data processing allowed the derivation of the atmospherically corrected Rrs(λ) as the input L2 product for the subsequent fixed threshold tests. In detail, the MSI-L1C data were re-sampled to a 10 m pixel size by the nearest neighbor technique and were atmospherically corrected via the multi-band "dark spectrum fitting" (DSF) method [57]. All the DSF setting options adopted in [16] were also implemented in this work for a faithful export of the method. In particular, the retrieval of the atmospheric path reflectance was performed by dividing the scene into 6 × 6 km tiles and thus considering the interpolated values to better account for the atmospheric

heterogeneity over the scene [16]. Furthermore, a user-tunable sun glint correction was applied through a SWIR-based threshold (any reflectance at 1.6 μm ≥ 0.11 was excluded).

After deriving Rrs(*λ*), a combination of fixed threshold tests was performed to mask the non-water pixels. Four spectral tests were implemented, as follows:

- The first was the "Bright" spectral test:

$$\boldsymbol{Rrs(\lambda)\,max > 0.2} \quad (2)$$

where:

Rrs(λ) max is the maximum value of Rrs(λ).

- The second was the "NIR peak" spectral test:

$$\boldsymbol{Max\,(Rrs_{BLUE}, Rrs_{GREEN}, Rrs_{RED}) < Rrs_{NIR}} \quad (3)$$

where:

Rrs $_{BLUE}$, Rrs $_{GREEN}$, Rrs $_{RED}$, and Rrs $_{NIR}$ refer to 0.443, 0.560, 0.704, and 0.833 μm central wavelengths, respectively.

- The third was the "Non-water" spectral test:

$$\boldsymbol{\frac{Rrs_{NIR}}{Rrs_{RED}} > 0.9\ AND\ Rrs_{NIR} > 0.05} \quad (4)$$

where:

Rrs $_{RED}$ and Rrs $_{NIR}$ refer to 0.704 and 0.833 μm, respectively.

- The fourth was the "White" spectral test:

$$\boldsymbol{\frac{Rrs\,(\lambda)max - Rrs(\lambda)min}{Rrs(\lambda)max} < 0.2} \quad (5)$$

where:

Rrs(λ) max and Rrs(λ) min refer to the maximum and minimum values of Rrs(λ).

The implementation of such tests and computing thresholds on the two satellite images (i.e., pre- and post-event) allowed the identification of the non-water pixels to be masked. In particular, the data were masked if any one of the four spectral tests considered was set to true [16]. The final identification into flooded and non-affected pixels was obtained by applying a change detection scheme between the images after and before the flooding event. The time necessary for the whole process was 10 h [16].

3. Results

Here, the results achieved by the RST-FLOOD implementation as described in Section 2.2.2 to the Emilia Romagna flood event are reported.

RST-FLOOD Results

The RST-FLOOD technique was implemented on the Sentinel-2 MSI L2A post-event image reported in false color in Figure 1c. The unperturbed conditions, as mentioned before, are not represented by the pre-event image but are defined through the reference fields obtained from the multi-temporal analysis of the historical data (see Section 2.2.2). The results are presented in Figure 6, where the flooded areas (in blue) were identified and mapped considering anomalies at the pixel level associated to $\otimes_{NDSI}(x,y,t) > 2$. In the following, we can see the general situation of the inundated areas as of 23 May 2023.

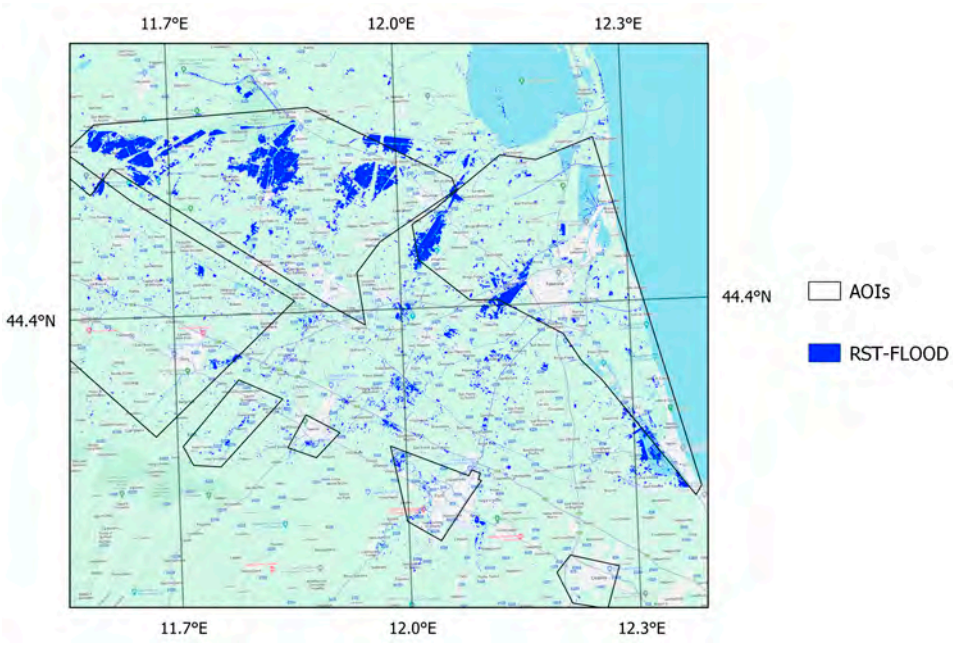

Figure 6. Flooded areas (in blue) identified by RST-FLOOD for Sentinel-2 L2A image of 23 May 2023. Black polygons are the different AOIs officially reported by the authorities. The Google Maps (world map service-WMS version) scene is used as the background.

The pixels detected by RST-FLOOD (in blue) are widely distributed on the whole analyzed scene: most of them fall within the principal AOIs (the black polygons) stated by the authorities during the emergency phase. The technique therefore appears to be efficient, demonstrating that it is able to detect and map the most affected areas. Other pixels, more or less extensively, are detected and are clearly visible outside these specific and already identified AOIs: this means the presence of further presumed floods, smaller in size than the others and distributed throughout the territory, which could indicate areas less involved but still affected by inundations. No in situ data are currently available for the Emilia Romagna event, which are necessary to carry out an efficient validation phase of what has just been presented, so the RST-FLOOD results have been evaluated and discussed in comparison with different sources of satellite technique/products.

4. Discussion

In order to assess the quality of the results obtained by exporting RST-FLOOD to the Sentinel-2 data in the following sections, they were compared with the same output coming from the independent CAB technique implementation of the same event/image and from the CEMS products presented in Section 2.2.1.

The main characteristics of the methodologies just mentioned are summarized in the next Table 1.

Table 1. Technical characteristics of the technique and products analyzed here.

Name	Data Type	Technique Type	Delivery Time
CAB	Optical Data	Semi-automatic	10 h
CEMS Delineation	SAR Data	Semi-automatic	18–34 h
CEMS R&R	SAR Data	Semi-automatic	2 months
RST-FLOOD	Optical Data	Fully automatic	15 min

4.1. CAB Technique Implementation and Comparison with RST-FLOOD

The CAB technique was implemented in this work to the Emilia Romagna flood event as described in Section 2.2.3. Two Sentinel-2 images were used, the one acquired after the

event on 23 May 2023 (Figure 1c) and the other one recorded in unperturbed conditions before the event, on 28 April 2023 (Figure 1b). The output map is shown in Figure 7, where the brown pixels delineate the identified flooded areas, while the black polygons are the different AOIs officially reported by the authorities.

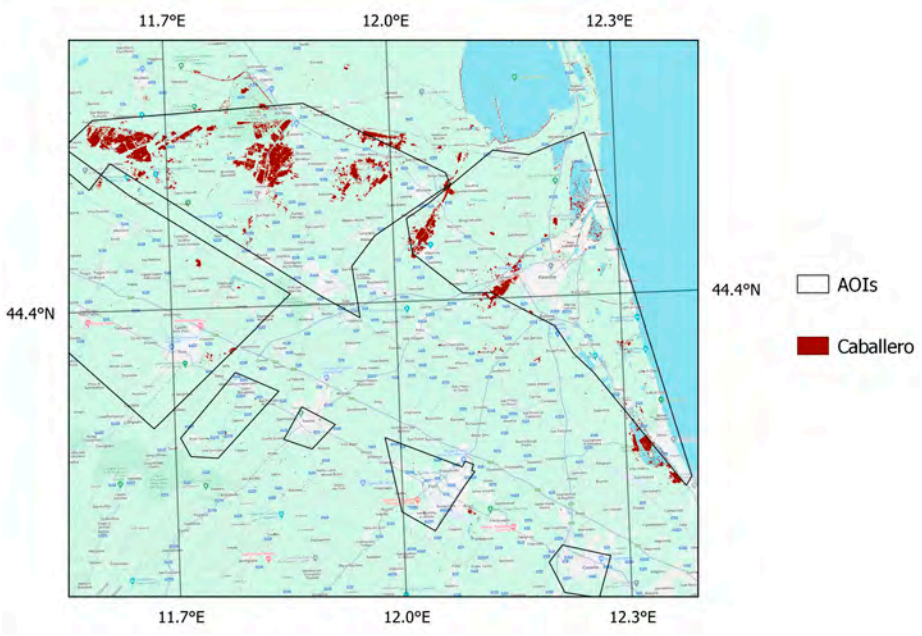

Figure 7. Flooded areas (in brown) identified applying [16] to the Sentinel-2 MSI image of 23 May 2023. Black polygons are the different AOIs officially reported by the authorities. The Google Maps (world map service-WMS version) scene is used as the background.

In order to evaluate the performance offered by the RST-FLOOD implementation when compared to a traditional fixed threshold technique like the one proposed by CAB, an overlap between the two is reported in the following Figure 8. The flooded areas identified only by RST-FLOOD are in blue, those only by CAB are in brown, while the areas reported by both of them are depicted in green. Some significant areas are shown in the magnified images in the same figure.

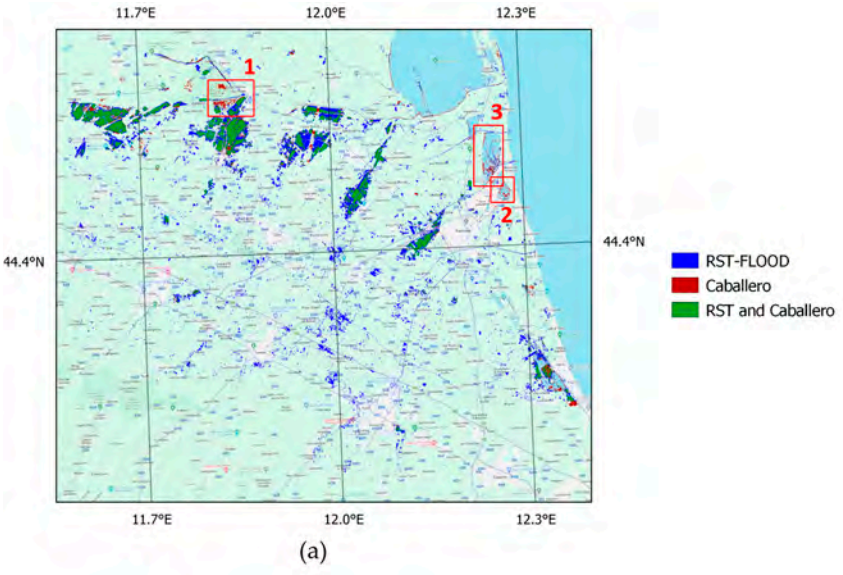

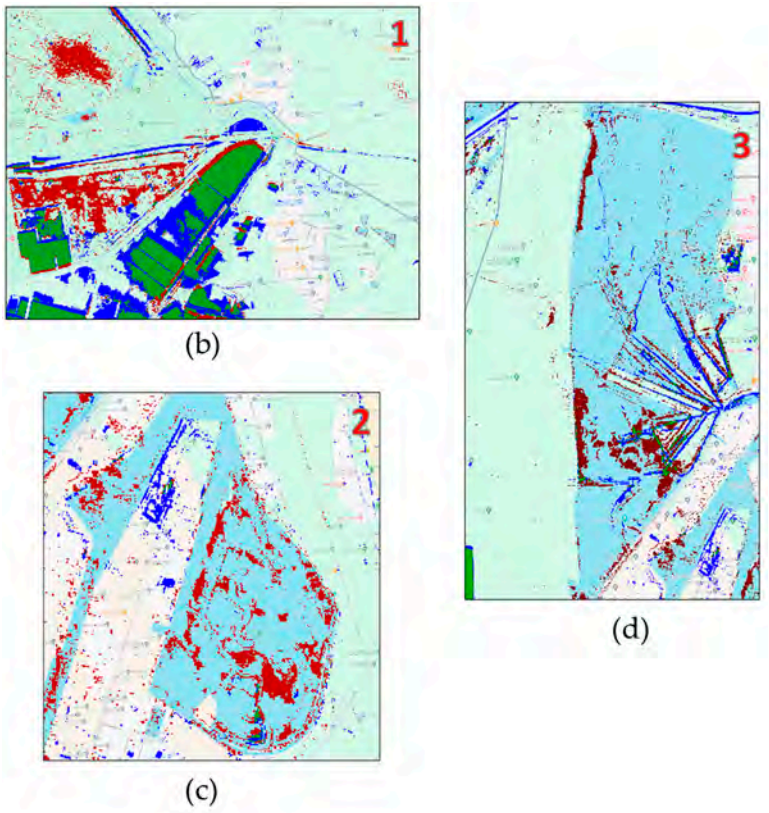

Figure 8. (**a**) Overlap between the RST-FLOOD and CAB maps; (**b**) magnified image of the Vallesanta area; (**c**) magnified image of the Pialassa dei Piomboni area; and (**d**) magnified image of the Pialassa della Baiona area. The Google Maps (world map service-WMS version) scene is used as the background.

In order to perform a quantitative comparison, all the flood-affected pixels identified by the two methods were considered separately, counting the common and exclusive detections. Therefore, the relative percentages were calculated, as reported in Table 2.

Table 2. Quantitative metrics relative to the RST-FLOOD and CAB comparison.

Flood Pixels Shared by Both Methods	RST-FLOOD Exclusive Detections	CAB Exclusive Detections
29.3%	58.9%	11.8%

The green pixel distribution in Figure 8a and the metrics reported in Table 2 (i.e., the flood pixels shared by both) demonstrate a quite good agreement between the two techniques in identifying the largest affected areas. However, some inconsistencies are also present and highlighted in Figure 8 as brown (i.e., the CAB exclusive detections in Table 2) and blue (i.e., the RST-FLOOD exclusive detections in Table 2) pixels. Some examples of these mismatches are shown in Figure 8b,c, where it is possible to observe that brown pixels partially cover areas of permanent water bodies (identified in cyan on the Google Maps scene used as the background). In detail, in Figure 8b, CAB identified as a flooded part of the Vallesanta (FE, Italy) a natural oasis that belongs to the Argenta Valleys, a Special Protection Area (SPA) characterized by natural vast geomorphological basins [58]. Likewise, in Figure 8c, the subcoastal lagoon of the Pialassa dei Piomboni (RA, Italy) SPA [59] is erroneously flagged as inundated.

Through these examples, it is clear that the CAB technique suffers from some limitations: the use of fixed non-adaptive thresholds does not allow an accurate differentiation between permanent water bodies and newly inundated areas on a single image; in addition, the simple change detection phase (exploiting the pre- and post-event images) may

lead to recognizing and reporting signal variations due to cyclic/seasonal phenomena that occur on the water surface (e.g., algal blooms), which are expected and are not related to an event occurrence. RST-FLOOD does not suffer from such limitations, because it does not work with fixed limit values and identifies the observed signal variation, comparing it with an expected value obtained through a historical analysis of the signal itself (see Section 2.2.2), rather than a single reference image.

Moving to another similar situation, in Figure 8d, the natural area of Pialassa della Baiona (RA) is shown: this area is a complex system connected by artificial canals and made up of seawater basins and freshwater ponds [60]. Within the basin in the figure, there are both brown pixels, corresponding to CAB exclusive identifications, and blue pixels, which relate to RST-FLOOD exclusive detections, which are mostly concentrated along the artificial canals and partially within the basin. In this case, the anomalies detected by RST-FLOOD are likely related to the presence of a large amount of sediment transported by the rivers during the previous rain events, which lead to a signal increase in the RED band resulting in the significantly positive values of the NDSI index compared to normal ones.

There are then other areas reported as floods only by RST-FLOOD (blue pixels). These areas are mostly located in the central and southern parts of the map, far from the largest inundated zones, identified well by both techniques (in green), but along the way of the rivers and waterways that overflowed during the event. Focusing on some of these spot areas (Figure 9a,b), it is possible to see that the blue pixels redraw the rivers and irrigation canals that typically lap the fields in this region, highlighting the realistic breaking of the banks and the flooding of the nearby fields.

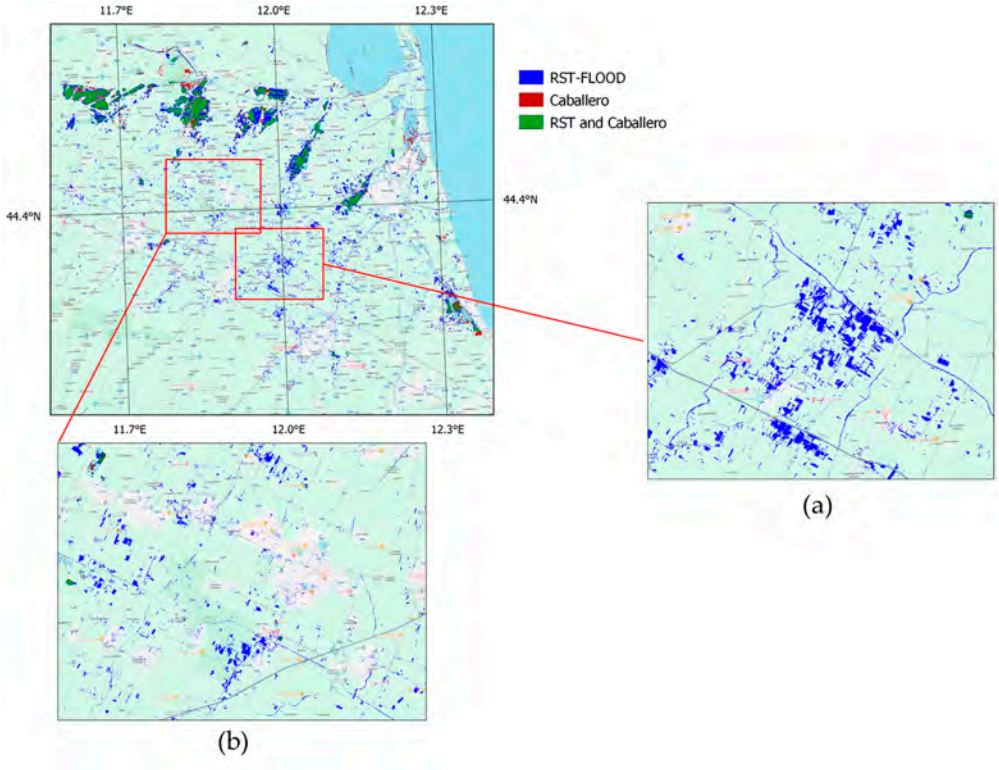

Figure 9. RST-FLOOD vs. CAB maps. (**a**,**b**) Magnified images of the spot fields reported as floods only by RST-FLOOD. The Google Maps (world map service-WMS version) scene is used as the background.

In order to better clarify the situation just described, a deeper analysis of some of these spotted areas was carried out. In the absence of in situ ground truth data, a sort of validation of the observed data was performed through the following procedure. After

having identified some control points (numbered in Figure 10) chosen as examples of the areas exclusively reported by RST-FLOOD, a historical analysis was implemented on each of them in terms of the land cover variation and, in particular, in terms of the Normalized Difference Vegetation Index (NDVI) [61]. The NDVI returns a different value depending on the land cover observed and its relative spectral response [62], moving in a range between −1 and 1: the highest positive values are related to vegetation presence and the negative ones are related to water, while the intermediate ones are representative of bare soil (a low positive) and clouds (around 0). Studying the historical index variation is useful to obtain information on how the land cover has changed during time and at a given point. The NDVI was computed as the normalized difference between the Sentinel-2 MSI L2A Near-InfraRed (NIR) (0.8 μm) and RED (0.4 μm) bands, i.e., (NIR-RED)/(NIR+RED), and it was implemented for all of May's data from 2017 to 2023. The results obtained for the control points identified are reported in the following Figure 10a–f.

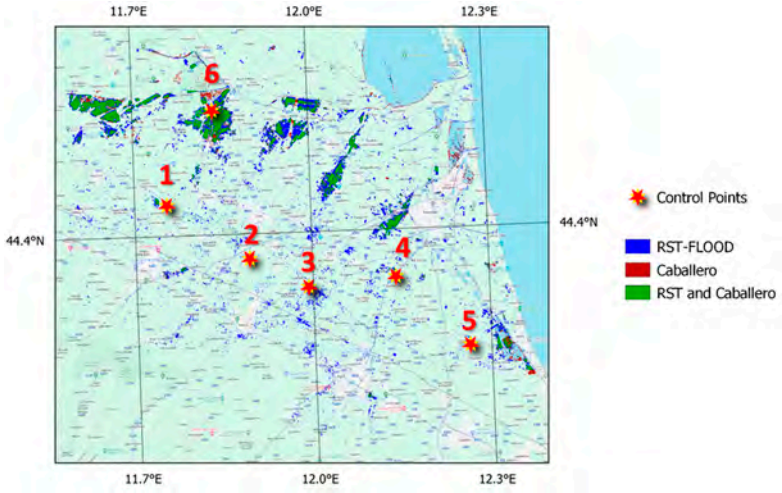

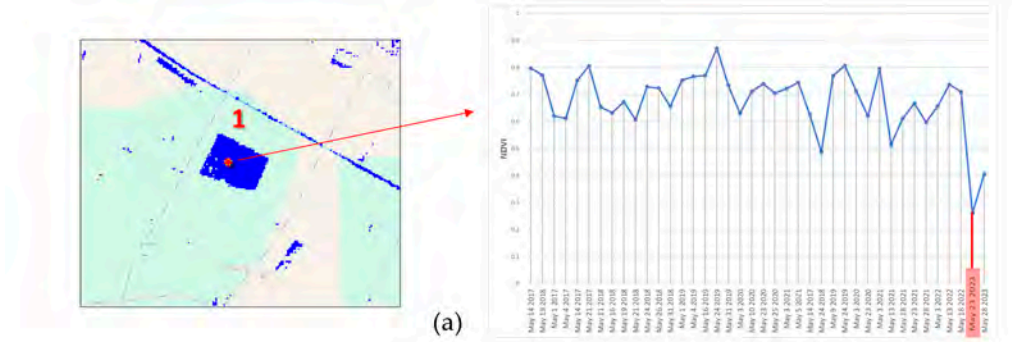

(a)

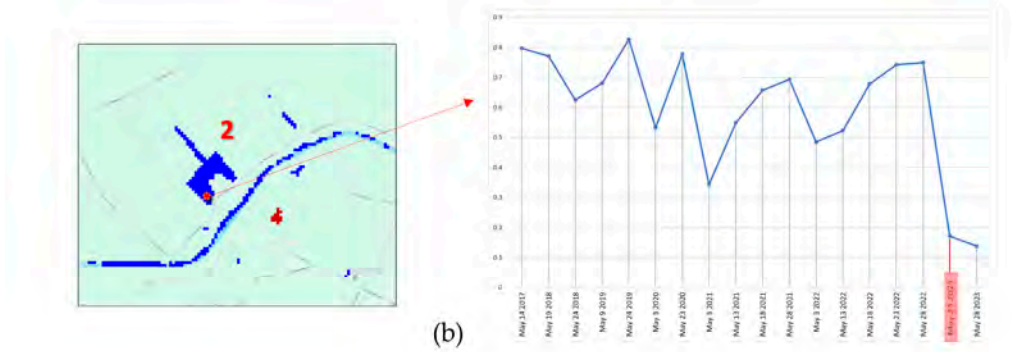

(b)

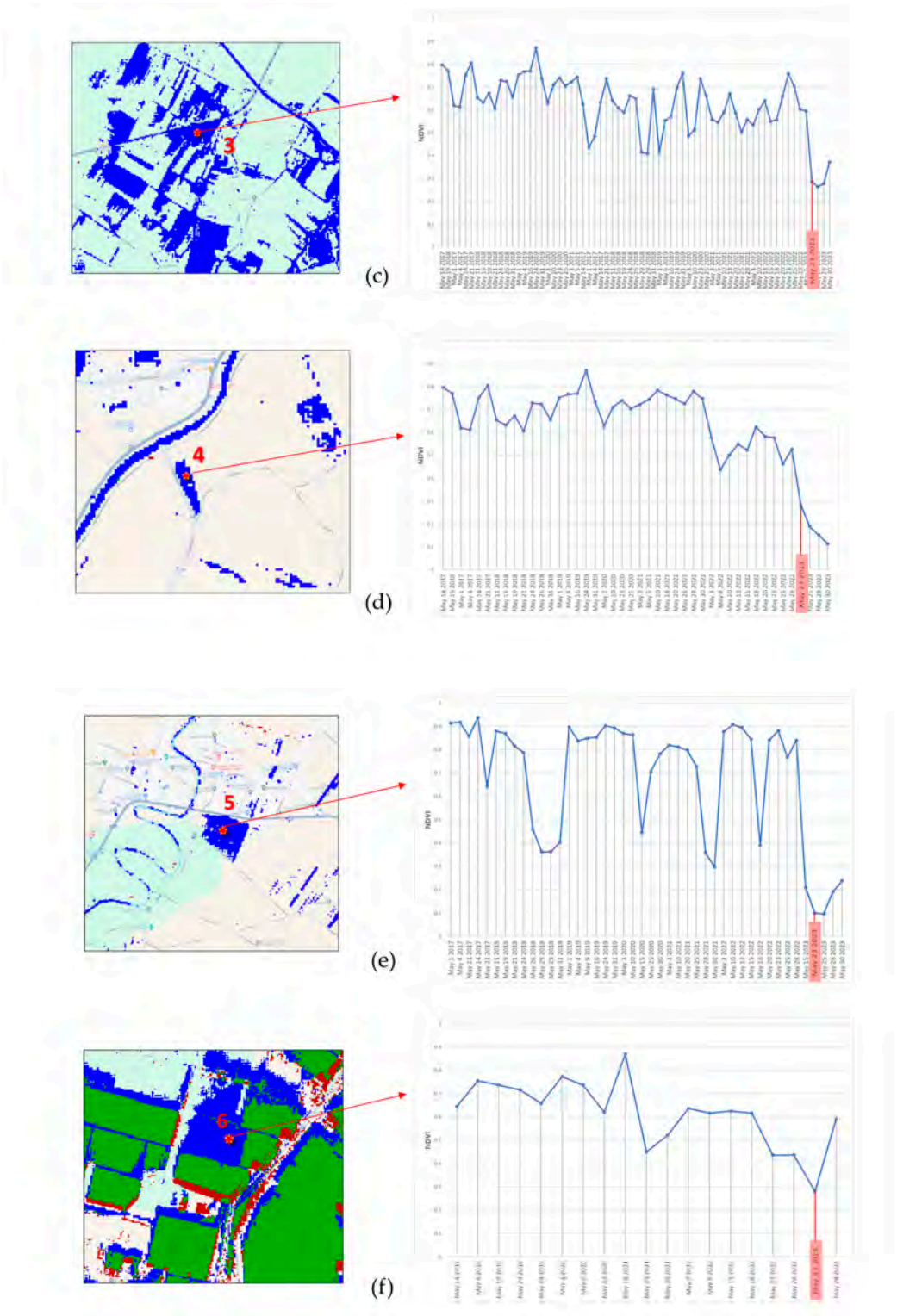

Figure 10. Location of control points identified as representative of the RST-FLOOD exclusive detections and the relative results of the NDVI historical analysis for (**a**) point 1, (**b**) point 2, (**c**) point 3, (**d**) point 4, (**e**) point 5, and (**f**) point 6. The Google Maps (world map service-WMS version) scene is used as the image background.

Looking at the NDVI temporal trend graph for each point reported (Figure 10a–f), it is worth noting a similar behavior for all of them: the NDVI values remain within a very small variation range over time, and the situation changes only on 23 May 2023 when, for

all the control points, a sharp drop in the index value is observed. These behaviors just described highlight how the land cover on each observed surface has remained almost the same over time, with small variations mainly due to a greater/lesser vegetation lushness or to some changes in the cultivation of the area. The sudden decrease registered on 23 May 2023 shows how the normal land cover was likely perturbed by the water presence, with a strong reduction in the NDVI values.

At the end of this analysis, which was carried out by choosing different control points in different areas and conditions in order to make the results as general as possible, it is clear that the RST-FLOOD technique is able to even locate areas covered by smaller water surfaces, demonstrating a greater sensitivity than CAB.

It is interesting to focus on the last control point shown in Figure 10f, which represents a slightly different situation than the others: in this case, the RST-FLOOD exclusive detection (the blue area) is close to the one shared with CAB (the green area). The relative NDVI trend demonstrates the correct water identification in the area, thus highlighting a greater sensitivity of the RST technique in delimiting even the full-blown flooded areas. This high accuracy can be seen not only in the area just shown but also around all the areas recognized as flooded by both techniques and reported in green in the previous Figures 9 and 10.

In summary, RST-FLOOD, even though it has some issues, appears to be more accurate and sensitive than a traditional approach technique, such as the here-analyzed CAB one. The result achieved by RST-FLOOD is, in addition, faster (15 min from satellite image availability) with respect to the one declared in [16] (10 h from satellite image availability), which makes it more suitable for use in emergency phases to rapidly return useful information.

4.2. Comparison between RST-FLOOD and CEMS Products

RST-FLOOD was also compared with the products generated starting from a different source of satellite data, i.e., the SAR microwave one provided by the official CEMS service, both in the rapid mapping and risk and recovery configurations. These two comparisons are particularly important to test the performance of the technique presented here when compared with the independent outputs produced as quickly as possible (CEMS rapid mapping) and with the greatest possible detail (CEMS risk and recovery).

In Figure 11, the overlap between the RST-FLOOD and CEMS *rapid mapping* delineation product presented in Section 2.2.1 is shown: here, the outputs of the first technique are in blue, those produced by the second one are in purple, and the results shared by both are in green.

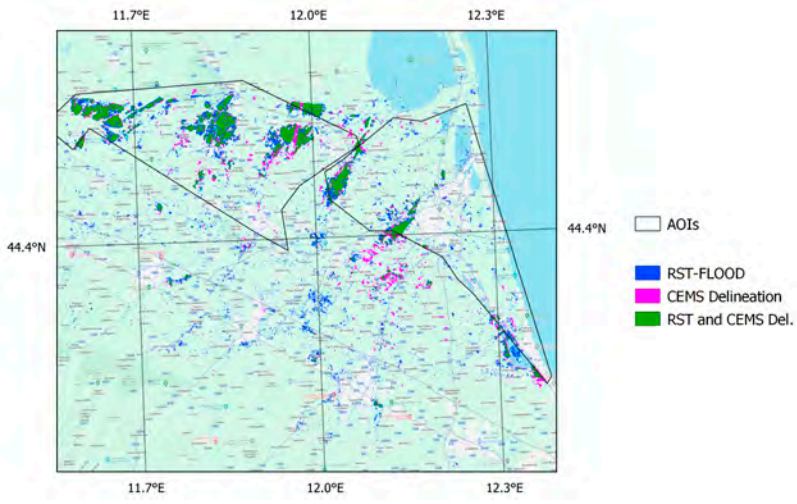

Figure 11. Overlap between RST-FLOOD (in blue) and CEMS delineation product (in purple) maps. The Google Maps (world map service-WMS version) scene is used as the background.

In this case, it is worth noting that the two maps are representative of different days and situations; in particular, the delineation map relates to 21 May 2023 while RST-FLOOD derives from 23 May 2023. In order to make the comparison as realistic as possible, the match between the RST-FLOOD technique and the CEMS delineation was verified and discussed for the largest affected areas, i.e., those where major changes were unlikely to occur in such a short time and, in particular, the ones within the 02-Lugo and 07-Ravenna AOIs (see Figure 3). In Figure 11, these areas are reported as black polygons and here the two independent outputs show a good agreement, with the most affected areas depicted in green to represent a detection shared by both the RST-FLOOD and CEMS delineation products. However, close to the extent of these greens, some inconsistences are present (purple or blue pixels), which are difficult to justify due to the different acquisition times of the relative source data. From a broader perspective, the RST-FLOOD returning information is almost completely comparable in terms of sensitivity to those provided by rapid products like the CEMS one, demonstrating a high performance.

In order to assess the accuracy with which this information has been provided, a second CEMS product was used, the R&R one, which is defined as the most detailed between all the products produced by the service. In this case, the satellite image used to retrieve the relative R&R map was acquired on 23 May 2023, the same day of the Sentinel-2 data used for RST-FLOOD, and this allows for a better comparison between them. The results of the two methods are shown in Figure 11, where the joint detections are in green and the RST-FLOOD exclusive identifications in blue, while the CEMS R&R recordings are in orange.

The two products agree quite well over the largest affected areas, as confirmed by the wide green areas in Figure 12. Looking at the rest of the scene, other considerations can be drawn: unlike the CAB product, the CEMS R&R map also reports a certain number of floods in the central and southern parts of the map (Figure 13). In detail, in Figure 13a,b the same areas already highlighted in Figure 9a,b are shown.

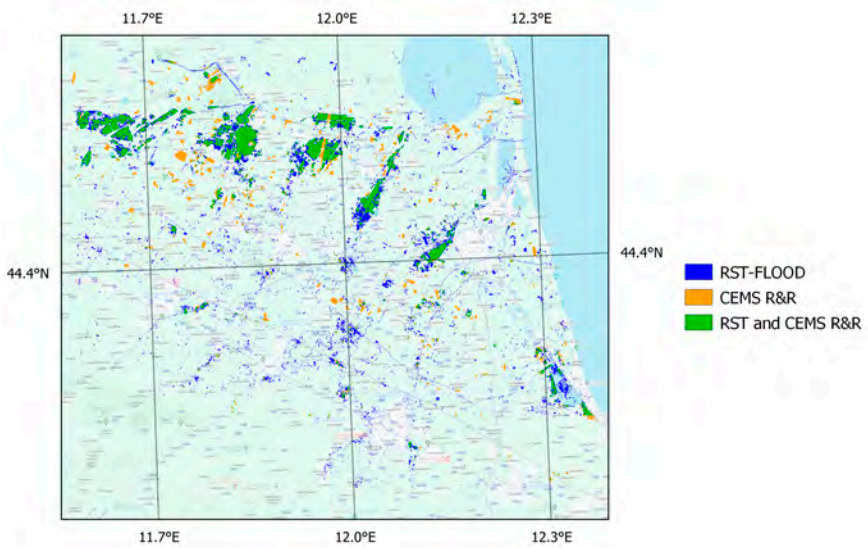

Figure 12. Overlap between the RST-FLOOD and CEMS risk and recovery product maps. The Google Maps (world map service-WMS version) scene is used as the background.

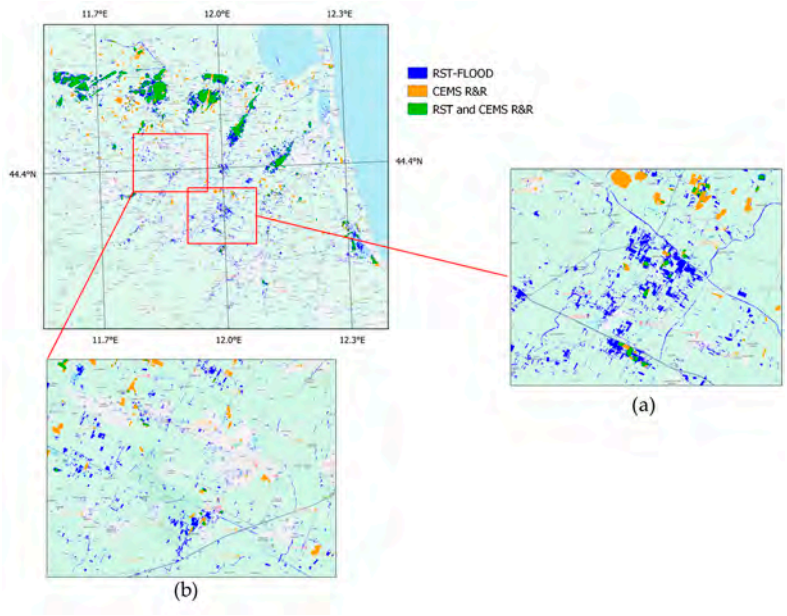

Figure 13. As in Figure 12 with (**a**,**b**) a magnified view of the spot fields reported in Figure 8a,b. The Google Maps scene is used as the background.

Some of those areas reported as floods exclusively by RST-FLOOD in Figure 9a,b are now matched with the CEMS R&R in Figure 13a,b and here depicted in green, confirming again the sensitivity of the method presented here. However, not all the RST-FLOOD detections match the CEMS ones, but these cases are mostly the same as already presented and discussed in Section 4.1, Figure 10, where the effectiveness of the technique was amply demonstrated.

It is also worth noting in Figure 12 the presence of some exclusive detections made by CEMS R&R (in orange): in order to better clarify these situations, the same procedure explained before for the match with the CAB technique was carried out. Some representative points were selected and then analyzed through the construction of the relative NDVI historical trend (Figure 14).

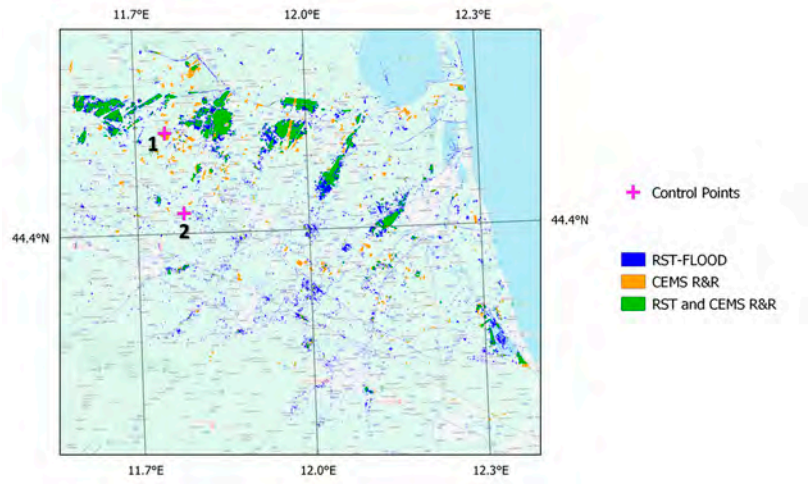

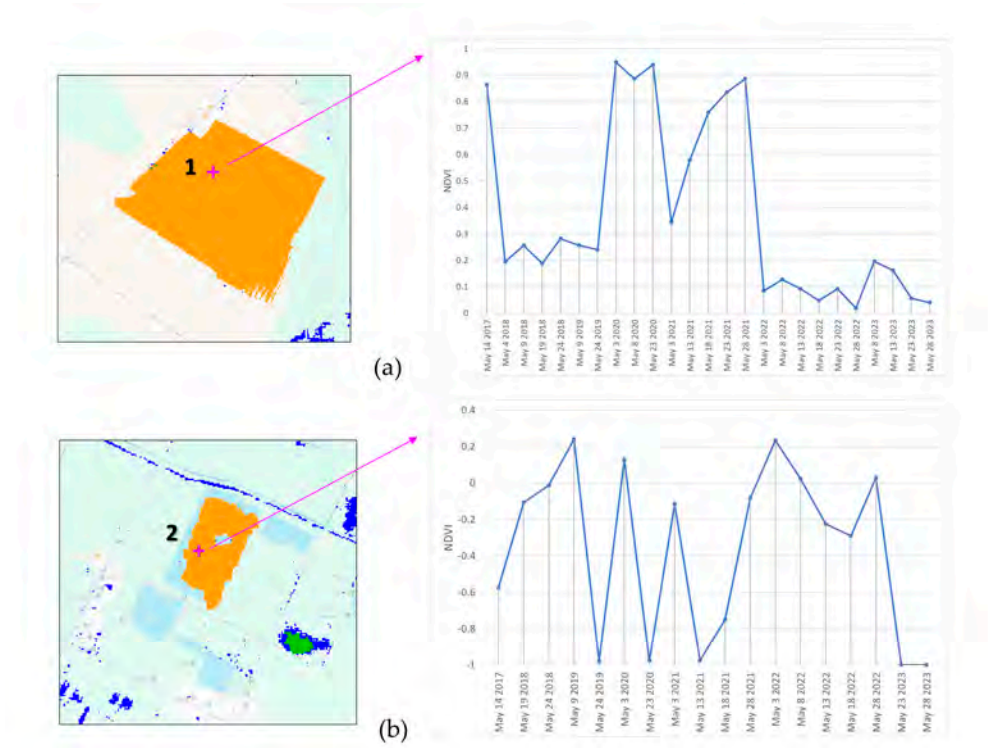

Figure 14. Location of the control points identified as representative of CEMS R&R exclusive detections and the relative results of the NDVI historical analysis for (**a**) point 1, and (**b**) point 2. The Google Maps (world map service-WMS version) scene is used as the image background.

The first control point (Figure 14a) was selected as an example of the isolated field reported as water-covered by the CEMS R&R and located far from the largest inundated areas: the NDVI trend in Figure 14a shows fluctuating values along the whole historical period, which could probably be attributable to crop rotation. It is possible to note a sudden NDVI decrease at the beginning of May 2022, which then remains almost the same the next times, with no significant value variation on 23 May 2023, the time of the flood event occurrence. The second control point (Figure 14b) is another example of an isolated area reported as a flood: the NDVI trend, in this case, takes values ranging between very low negative ones (−1) and slightly greater than 0 ones, suggesting that this is not a new inundated area but rather a permanent water body, as also testified by the Google Maps scene in the background.

The analysis that was carried out and that has just been presented allowed us to understand that in these cases RST-FLOOD does not make any sensitivity errors but testifies that some lack in accuracy (in terms of false identifications returned) is therefore made by the most reliable product produced by the official service. It is the CEMS itself that highlights some limitations of the R&R flood delineation product [45]: they are mainly related to the interpretability of the used SAR image, due, as an example, to the vegetation presence, which backscatters the microwave signal before reaching the soil, together with the scattering mechanisms and SAR geometric effects occurring in an urban environment, which affect the correct detection, resulting in an underestimation of the total flood extent [45].

At the end of all the considerations just made, it is possible to conclude that the RST-FLOOD technique, despite the simplicity and automaticity of its implementation, returns a precise mapping in rapid mode, with such sensitivity as to be able to quickly return useful information and with a better degree of accuracy than that which is currently achieved after months of analysis. However, the main drawback of the optical band, due to the lack of information on the presence of clouds, may limit the applicability of the RST-FLOOD technique. Therefore, its integration with other active SAR-based monitoring

techniques during crisis phases would improve the accuracy, sensitivity, and timeliness of the provided information.

5. Conclusions

Flash floods are nowadays widespread phenomena, which occur at any latitude with devasting consequences for human life and nature. Timely information about ongoing emergency phases are crucial to manage the crisis, protect the environment, and save human lives. In this paper, an existing satellite-based unsupervised technique for automatic flood detection and mapping, namely RST-FLOOD [34], was ported for the first time to mid–high-spatial resolution (20 m) Sentinel-2 MSI data. Its characteristics and main strengths, i.e., its implementation speed and lack of need for fixed threshold values, were tested on the recent Emilia Romagna (Italy) flood event that occurred in May 2023. The performance and quality of the final product were evaluated and discussed together with the results obtained by an independent optical technique developed in [16] and here implemented to the study case and the official SAR-based flood delineation products provided by the CEMS service for the same event.

RST-FLOOD was demonstrated to be more accurate and sensitive than traditional fixed threshold-based techniques, like the CAB one analyzed here, managing to recognize and map the affected areas with more effectiveness and also with a faster delivery time of the final product (i.e., only 15 min against 10 h declared by CAB).

A good performance was also showed when the technique was compared with the official SAR-based CEMS products, both in terms of the final map production speed and the accuracy of its content. RST-FLOOD, using the first post-event satellite images available, was able to delimit the most affected areas returning similar information in terms of sensitivity to those provided by the CEMS rapid mapping products but with an accuracy and degree of detail comparable and in some cases better than the CEMS R&R product obtained after a long two months of the data interpolation process and improvement of the analysis techniques.

In conclusion, RST-FLOOD, being effective and fast, is demonstrated to be a good analysis instrument, allowing an increase in the speed of the usability of accurate information on ongoing events, which currently take months to be released. However, due to the limitations of the optical band in the presence of clouds, a full and systematic integration of RST-FLOOD within larger monitoring systems based on different sources of data is recommended. Its own structure of using only satellite images without the need for ancillary data allows it to be easily exported and implemented in any geographical area with different characteristics without losing performance. The processing chain and full implementation within the GEE environment allows this global-scale implementation in a very fast mode.

Author Contributions: Methodology, V.T., N.P. and V.S.; software, V.S.; formal analysis, V.S. and E.C.; writing—original draft preparation, V.S. and E.C.; writing—review and editing, V.T. and N.P.; supervision, V.T. and N.P.; and funding acquisition, V.T. All authors have read and agreed to the published version of this manuscript.

Funding: This research was supported by the MIUR PON R&I 2014–2020 Program (project MITIGO, ARS01_00964).

Data Availability Statement: All the data used to implement RST-FLOOD within Google Earth Engine platform are available in the Earth Engine public catalogue (i.e. https://developers.google.com/earth-engine/datasets/catalog/sentinel)

Conflicts of Interest: The authors declare no conflicts of interest.

References

1. Hapuarachchi, H.A.P.; Wang, Q.J.; Pagano, T.C. A review of advances in flash flood forecasting. *Hydrol. Process.* **2011**, *25*, 2771–2784. https://doi.org/10.1002/hyp.8040.
2. Markert, K.L.; Chishtie, F.; Anderson, E.R.; Saah, D.; Griffin, R.E. On the merging of optical and SAR satellite imagery for surface water mapping applications. *Results Phys.* **2018**, *9*, 275–277. https://doi.org/10.1016/j.rinp.2018.02.054.
3. Dasgupta, A.; Grimaldi, S.; Ramsankaran, R.; Pauwels, V.R.N.; Walker, J.P.; Chini, M.; Hostache, R.; Matgen, P. Flood Mapping Using Synthetic Aperture Radar Sensors from Local to Global Scales. In *Global Flood Hazard: Applications in Modeling, Mapping, and Forecasting, Geophysical Monograph 233*, 1st ed.; John Wiley & Sons, Inc.: Hoboken, NJ, USA, **2018**; ISBN 978-1-119-21786-2.
4. Foroughnia, F.; Alfieri, S.M.; Menenti, M.; Lindenbergh, R. Evaluation of SAR and Optical Data for Flood Delineation Using Supervised and Unsupervised Classification. *Remote Sens.* **2022**, *14*, 3718. https://doi.org/10.3390/rs14153718.
5. Colosio, P.; Tedesco, M.; Tellman, E. Flood Monitoring Using Enhanced Resolution Passive Microwave Data: A Test Case over Bangladesh. *Remote Sens.* **2022**, *14*, 1180. https://doi.org/10.3390/rs14051180.
6. Amitrano, D.; Di Martino, G.; Di Simone, A.; Imperatore, P. Flood Detection with SAR: A Review of Techniques and Datasets. Remote Sensing. **2024**; 16(4):656. https://doi.org/10.3390/rs16040656
7. Bauer-Marschallinger, B.; Cao, S.; Tupas, M.E.; Roth, F.; Navacchi, C.; Melzer, T.; Freeman, V.; Wagner, W. Satellite-Based Flood Mapping through Bayesian Inference from a Sentinel-1 SAR Datacube. *Remote Sens.* **2022**, *14*, 3673. https://doi.org/10.3390/rs14153673.
8. Schlaffer, S.; Matgen, P.; Hollaus, M.; Wagner, W. Flood detection from multi-temporal SAR data using harmonic analysis and change detection. *Int. J. Appl. Earth Obs. Geoinf.* **2015**, *38*, 15–24. https://doi.org/10.1016/j.jag.2014.12.001.
9. Li, S.; Sun, D.; Goldberg, M.D.; Sjoberg, B.; Santek, D.; Hoffman, J.P.; DeWeese, M.; Restrepo, P.; Lindsey, S.; Holloway, E. Automatic near real-time flood detection using Suomi-NPP/VIIRS data. *Remote Sens. Environ.* **2018**, *204*, 672–689. https://doi.org/10.1016/j.rse.2017.09.032.
10. Huang, C.; Chen, Y.; Zhang, S.; Wu, J. Detecting, extracting, and monitoring surface water from space using optical sensors: A review. *Rev. Geophys.* **2018**, *56*, 333–360. https://doi.org/10.1029/2018RG000598.
11. Faruolo, M.; Coviello, I.; Lacava, T.; Pergola, N.; Tramutoli, V. A multi-sensor exportable approach for automatic flooded areas detection and monitoring by a composite satellite constellation. *IEEE Trans. Geosci. Remote Sens.* **2013**, *51*, 2136–2149. https://doi.org/10.1109/TGRS.2012.2236336.
12. Fayne, J.; Bolten, J.; Lakshmi, V.; Ahamed, A. Optical and Physical Methods for Mapping Flooding with Satellite Imagery. In *Remote Sensing of Hydrological Extremes; Springer Remote Sensing/Photogrammetry*; Lakshmi, V., Ed.; Springer International Publishing: Basel, Switzerland, 2017; Chapter 5, pp. 83–103. https://doi.org/10.1007/978-3-319-43744-6_5.
13. Kwak, Y. Nationwide Flood Monitoring for Disaster Risk Reduction Using Multiple Satellite Data. *ISPRS Int. J. Geo-Inf.* **2017**, *6*, 203. https://doi.org/10.3390/ijgi6070203.
14. Ogilvie, A.; Belaud, G.; Massuel, S.; Mulligan, M.; Le Goulven, P.; Calvez, R. Surface water monitoring in small water bodies: Potential and limits of multi-sensor Landsat time series. *Hydrol. Earth Syst. Sci.* **2018**, *22*, 4349–4380. https://doi.org/10.5194/hess-22-4349-2018.
15. Cavallo, C.; Papa, M.N.; Gargiulo, M.; Palau-Salvador, G.; Vezza, P.; Ruello, G. Continuous Monitoring of the Flooding Dynamics in the Albufera Wetland (Spain) by Landsat-8 and Sentinel-2 Datasets. *Remote Sens*. **2021**, *13*, 3525. https://doi.org/10.3390/rs13173525.
16. Caballero, I.; Ruiz, J.; Navarro, G. Sentinel-2 satellites provide near-real time evaluation of catastrophic floods in the west mediterranean. *Water* **2019**, *11*, 2499. https://doi.org/10.3390/w11122499.
17. Goffi, A.; Stroppiana, D.; Brivio, P.A.; Bordogna, G.; Boschetti, M. Towards an automated approach to map flooded areas from Sentinel-2 MSI data and soft integration of water spectral features. *Int. J. Appl. Earth Obs. Geoinf.* **2020**, *84*, 101951. https://doi.org/10.1016/j.jag.2019.101951.
18. Marc, W.; Martinis, S. A modular processing chain for automated flood monitoring from multi-spectral satellite data. *Remote Sens.* **2020**, *11*, 2330. https://doi.org/10.3390/rs11192330.
19. Copernicus Sentinel-1 Mission. Available online: https://sentinels.copernicus.eu/web/sentinel/missions/sentinel-1 (accessed on 18 July 2024).
20. Chang, S.; Deng, Y.; Zhang, Y.; Zhao, Q.; Wang, R.; Zhang, K. An advanced scheme for range ambiguity suppression of spaceborne SAR based on blind source separation. *IEEE Trans. Geosci. Remote Sens.* **2022**, *60*, 1–12. https://doi.org/10.1109/TGRS.2022.3184709.
21. Pradhan, B.; Tehrany, M.S.; Jebur, M.N. A New Semiautomated Detection Mapping of Flood Extent from TerraSAR-X Satellite Image Using Rule-Based Classification and Taguchi Optimization Techniques. *IEEE Trans. Geosci. Remote Sens.* **2016**, *54*, 4331–4342. https://doi.org/10.1109/TGRS.2016.2539957.
22. Salamon, P.; Mctlormick, N.; Reimer, C.; Clarke, T.; Bauer-Marschallinger, B.; Wagner, W.; Martinis, S.; Chow, C.; Böhnke, C.; Matgen, P.; et al. The New, Systematic Global Flood Monitoring Product of the Copernicus Emergency Management Service. In Proceedings of the 2021 IEEE International Geoscience and Remote Sensing Symposium IGARSS, Brussels, Belgium, 11–16 July 2021; IEEE: Piscataway, NJ, USA, 2021; pp. 1053–1056. https://doi.org/10.1109/IGARSS47720.2021.9554214.
23. Global Flood Awareness System (GloFAS) for Copernicus Emergency Management Service (CEMS). Available online: https://global-flood.emergency.copernicus.eu/ (accessed on 17 September 2024).

24. Schumann, G.P.; Brakenridge, G.R.; Kettner, A.J.; Kashif, R.; Niebuhr, E. Assisting Flood Disaster Response with Earth Observation Data and Products: A Critical Assessment. *Remote Sens.* **2018**, *10*, 1230. https://doi.org/10.3390/rs10081230.
25. Wang, Q.; Watanabe, M.; Hayashi, S.; Murakami, S. Using NOAA AVHRR data to assess flood damage in China. *Environ. Monit. Assess.* **2003**, *82*, 119–148. https://doi.org/10.1023/A:1021898531229.
26. Jain, S.K.; Saraf, A.K.; Goswami, A.; Ahmad, T. Flood inundation mapping using NOAA AVHRR data. *Water Resour. Manag.* **2006**, *20*, 949–959. https://doi.org/10.1007/s11269-006-9016-4.
27. Rahman, M. S.; Di, L. The state of the art of spaceborne remote sensing in flood management. Natural Hazards, **2017**, 85, 1223-1248. https://doi.org/10.1007/s11069-016-2601-9
28. Brakenridge, R.; Anderson, E. MODIS-based flood detection, mapping and measurement: The potential for operational hydrological applications. In *Transboundary Floods: Reducing Risks through Flood Management*; Springer: Dutch, The Netherlands, 2006; pp. 1–12. https://doi.org/10.1007/1-4020-4902-1_1.
29. Ahamed, A.; Bolten, J.D. A MODIS-based automated flood monitoring system for southeast asia. *Int. J. Appl. Earth Obs. Geoinf.* **2017**, *61*, 104–117. https://doi.org/10.1016/j.jag.2017.05.006.
30. Copernicus Web Site Available online https://sentinels.copernicus.eu/web/sentinel/home (accessed on 17 September 2024).
31. Copernicus Emergency Management Service Website. Available online: https://emergency.copernicus.eu/ (accessed on 18 July 2024).
32. CEMS Rapid Mapping Portfolio. Available online: https://emergency.copernicus.eu/mapping/ems/rapid-mapping-portfolio (accessed on 18 July 2024).
33. CEMS Risk and Recovery Portfolio. Available online: https://emergency.copernicus.eu/mapping/ems/risk-and-recovery-mapping-portfolio (accessed on 18 July 2024).
34. Lacava, T.; Ciancia, E.; Faruolo, M.; Pergola, N.; Satriano, V.; Tramutoli, V. On the potential of RST-FLOOD on visible infrared imaging radiometer suite data for flooded areas detection. *Remote Sens.* **2019**, *11*, 598. https://doi.org/10.3390/rs11050598.
35. Lacava, T.; Filizzola, C.; Pergola, N.; Sannazzaro, F.; Tramutoli, V. Improving flood monitoring by the Robust AVHRR Technique (RAT) approach: The case of the April 2000 Hungary flood. *Int. J. Remote Sens.* **2010**, *31*, 2043–2062. https://doi.org/10.1080/01431160902942902.
36. Valente, M.; Zanellati, M.; Facci, G.; Zanna, N.; Petrone, E.; Moretti, E.; Ragazzoni, L. Health System Response to the 2023 Floods in Emilia-Romagna, Italy: A Field Report. *Prehospital Disaster Med.* **2023**, *38*, 813–817. https://doi.org/10.1017/S1049023X23006404.
37. Agenzia per la Sicurezza Territoriale e Protezione Civile. Available online: https://protezionecivile.regione.emilia-romagna.it/notizie/2023/maggio/copy_of_alluvione-sanita-proroga-pagamenti (accessed on 18 July 2024).
38. Il Resto del Carlino Journal Website. Available online: https://www.ilrestodelcarlino.it/emilia-romagna/cronaca/alluvione-emilia-romagna-numeri-cml6u604 (accessed on 18 July 2024).
39. Agenzia per la Sicurezza Territoriale e Protezione Civile. Available online: https://protezionecivile.regione.emilia-romagna.it/notizie/2023/maggio/36000-persone-evacuate-20-maggio-allagamenti-aggiuntivi-a-ravenna (accessed on 18 July 2024).
40. Copernicus Sentinel-2 Mission. Available online: https://sentinels.copernicus.eu/web/sentinel/missions/sentinel-2 (accessed on 18 July 2024).
41. Copernicus Sentinel-2 User Guide. Available online: https://sentinels.copernicus.eu/web/sentinel/user-guides/sentinel-2-msi (accessed on 18 July 2024).
42. Copernicus Sentinel-2 Data Products. Available online: https://sentinels.copernicus.eu/web/sentinel/missions/sentinel-2/data-products (accessed on 18 July 2024).
43. Copernicus Sentinel-2 Processing Levels. Available online: https://sentinel.esa.int/web/sentinel/user-guides/sentinel-2-msi/processing-levels/level-2 (accessed on 18 July 2024).
44. Copernicus Emergency Management Service (CEMS) Emilia Romagna Event. Available online: https://rapidmapping.emergency.copernicus.eu/EMSR664/download (accessed on 18 July 2024).
45. Technical Report for Emilia Romagna Event. Available online: https://emergency.copernicus.eu/mapping/list-of-components/EMSN154 (accessed on 18 July 2024).
46. Copernicus Emergency Management Service Bulletin. Available online: https://emergency.copernicus.eu/mapping/ems/information-bulletin-167-copernicus-emergency-management-service-activities-following-latest (accessed on 18 July 2024).
47. Tramutoli, V. Robust satellite techniques (RST) for natural and environmental hazards monitoring and mitigation: Theory and applications. In Proceedings of the 2007 International Workshop on the Analysis of Multi-Temporal Remote Sensing Images, Leuven, Belgium, 18–20 July 2007; IEEE: Piscataway, NJ, USA, 2007. https://doi.org/10.1109/MULTITEMP.2007.4293057.
48. Dozier, J. Spectral signature of alpine snow cover from the Landsat thematic mapper. *Remote Sens. Environ.* **1989**, *28*, 9–22. https://doi.org/10.1016/0034-4257(89)90101-6.
49. Google Earth Engine Website. Available online: https://earthengine.google.com/ (accessed on 18 July 2024).
50. Copernicus Sentinel-2 Harmonized Product Description on GEE. Available online: https://developers.google.com/earth-engine/datasets/catalog/COPERNICUS_S2_SR_HARMONIZED#bands; (accessed on 18 July 2024).
51. Copernicus Sentinel-2 Cloud Masks Description on GEE. Available online: https://sentinel.esa.int/web/sentinel/technical-guides/sentinel-2-msi/level-1c/cloud-masks (accessed on 18 July 2024).
52. Copernicus Sentinel-2 Cloud Probability Product Description on GEE. Available online: https://developers.google.com/earth-engine/datasets/catalog/COPERNICUS_S2_CLOUD_PROBABILITY (accessed on 18 July 2024).

53. Cuomo, V.; Filizzola, C.; Pergola, N.; Pietrapertosa, C.; Tramutoli, V. A self-sufficient approach for GERB cloudy radiance detection. *Atmos. Res.* **2004**, *72*, 39–56.
54. Pietrapertosa, C.; Pergola, N.; Lanorte, V.; Tramutoli, V. Self Adaptive Algorithms for Change Detection: OCA (the One-channel Cloud-detection Approach) an adjustable method for cloudy and clear radiances detection. In Proceedings of the Technical Proceedings of the Eleventh International (A)TOVS Study Conference (ITSC-XI), Budapest, Hungary, 20–26 September 2000; pp. 281–291. https://doi.org/10.1016/j.atmosres.2004.03.030.
55. Lacava, T.; Marchese, F.; Pergola, N.; Tramutoli, V.; Coviello, I.; Faruolo, M.; Paciello, R.; Mazzeo, G. RSTVOLC implementation on MODIS data for monitoring of thermal volcanic activity. *Ann. Geophys.* **2011**, *54(5)*. https://doi.org/10.4401/ag-5337.
56. ESA's Science Hub Web Portal. Available online: https://dataspace.copernicus.eu/. (accessed on 17 September 2024)
57. Vanhellemont, Q. Adaptation of the Dark Spectrum Fitting Atmospheric Correction for Aquatic Applications of the Landsat and Sentinel-2 Archives. *Remote Sens. Environ.* **2019**, *225*, 175–192. https://doi.org/10.1016/j.rse.2019.03.010.
58. Ente Parco del Po Website. Available online: https://www.parcodeltapo.it/it/IT4060001.php (accessed on 18 July 2024).
59. Ente Parco del Po Website. Available online: https://www.parcodeltapo.it/it/IT4070006.php (accessed on 18 July 2024).
60. Ravenna Tourism Website. Available online: https://www.turismo.ra.it/en/nature-seaside/natural-areas/pialassa-della-baiona/ (accessed on 18 July 2024).
61. Rouse, J.W.; Haas, R.H.; Schell, J.A.; Deering, D.W. Monitoring vegetation systems in the Great Plains with ERTS. In Proceedings of the ERTS-1 Symposium 3rd, NASA, Greenbelt, MD, USA, 10–14 December 1974.
62. Huang, S.; Tang, L.; Hupy, J.P.; Wang, Y.; Shao, G.F. A commentary review on the use of normalized difference vegetation index (NDVI) in the era of popular remote sensing. *J. For. Res.* **2021**, *32*, 1–6. https://doi.org/10.1007/s11676-020-01155-1.